applied sciences

MDPI

Article

Experimental Study and Numerical Analysis of Temperature Stress in Carbon Fiber-Heated Concrete Pavement

Nengqi Zhang, Zhi Chen *, Henglin Xiao, Lifei Zheng and Qiang Ma

School of Civil Engineering and Environment, Hubei University of Technology, Wuhan 430068, China; zhangnengqi990903@163.com (N.Z.); xiao-henglin@163.com (H.X.); lfeizheng@163.com (L.Z.); maqiang927@163.com (Q.M.)

* Correspondence: chenzhi1988420@126.com

Abstract: Carbon fiber heating technology has been widely used in pavement surfaces in practical engineering projects as an environmentally friendly, efficient, and safe ice melting technique. However, the current design of carbon fiber-heated pavement focuses primarily on the ice melting effect while neglecting the crucial mechanical performance evaluation. Therefore, this study aims to investigate the temperature and thermal strain distributions of concrete pavement through model tests and develop a corresponding three-dimensional numerical model to analyze the temperature stress field distribution of carbon fiber-heated pavement. The accuracy of the numerical model is verified by comparing the model test results with the numerical analysis results. The numerical model test results indicate that the maximum compressive stress near the carbon fiber wire is 4 MPa, while the maximum tensile stress between the two carbon fiber wires is 1 MPa. According to the design standard for highway cement concrete pavement, the temperature stress induced by temperature change is significantly lower than the design value of the material's inherent strength. In addition, a linear relationship between the depth and temperature gradient affecting temperature stress is observed after establishing a correlation between the temperature gradient and temperature stress. The findings of this study can provide valuable insight into the design of carbon fiber-heated concrete pavements.

Keywords: carbon fiber heating wire; concrete pavement; numerical analysis; temperature gradient; thermal strain; temperature stress

Citation: Zhang, N.; Chen, Z.; Xiao, H.; Zheng, L.; Ma, Q. Experimental Study and Numerical Analysis of Temperature Stress in Carbon Fiber-Heated Concrete Pavement. *Appl. Sci.* **2024**, *14*, 359. https://doi.org/10.3390/app14010359

Academic Editor: Yoong Ahm Kim

Received: 22 November 2023
Revised: 25 December 2023
Accepted: 29 December 2023
Published: 30 December 2023

1. Introduction

Snow and ice on highways have become a major cause of car accidents during the winter. To address this issue, numerous efforts have been made to melt snow and ice on roadways, the most common of which are chemical de-icing [1,2], geothermal de-icing [3,4], and electric de-icing [5,6]. The spraying of de-icing chemicals on the road to melt snow and ice is a chemical de-icing method that not only demands a lot of people and material resources, but also causes traffic congestion and traffic safety hazards. De-icing chemicals left on roads can cause corrosion damage to pavement structures when they seep into the road [7] and damage soil ecology when they seep into the soil [8,9]. In order to convey heat from underground heat sources to the road surface, the geothermal de-icing method entails laying circulation pipes on the road's surface. These pipes use gas or liquid as the circulation medium. However, this technology has more severe circulating media requirements, and the selection and installation of circulating pipes and subsurface heat exchange tubes is more difficult.

Electrothermal de-icing technology melts snow and ice by putting conductive material on road, bridge, and airport pavement and activating that material to generate heat by utilizing the conductive material's electrical resistance [10]. Because of the benefits of its easy building process, low cost, environmental protection, high efficiency, and stability, the

technology is extensively employed in actual projects. Carbon fiber heating wire is becoming increasingly extensively employed as a conductive material for snow and ice melting as technology advances. The investigation of road surface temperature stress is separated into two parts: temperature distribution and mechanical properties. In terms of temperature distribution, Vignisdottir [11] meticulously examined the impact of previous de-icing technologies on both the road and environment, establishing the long-term viability of electric heating as an environmentally beneficial de-icing technology. Zhao [12] investigated the de-icing impact of carbon fiber electric heating wire on concrete pavement using model testing and numerical experiments, establishing the feasibility of de-icing concrete pavement using carbon fiber electric heating wire as well as the benefits of cleanliness and environmental protection. Real-time de-icing is faster than previous procedures and demonstrates the advantages of carbon fiber over other heating wire materials, including it being lightweight and possessing high flexibility and high tensile strength. Lai [13] investigated the effect of heat flux on the ice melting effect of concrete pavement through model tests and suggested that the increase in heat flux can effectively reduce the total energy consumption of ice melting. Lai [14] established a full-scale model in the field for assessing the performance of the carbon fiber heating wire approach for snow melting on airport pavement, proposing that a nonlinear temperature gradient is formed inside the pavement during the heating process. Liu [15] proposed an electric heat pipe ice and snow melting pavement thermal field prediction model based on line heat source theory, considering the effects of burial spacing, burial depth, heating power, heating time, and ambient temperature on pavement temperature. Qin [16] developed a one-dimensional heat transfer model for pavement temperature distribution and evaluated the influence of air temperature on stiff paving slab temperature distribution along the depth direction. Gao [17] presented a three-dimensional finite element model for effectively forecasting the thermal behavior of fire-exposed RC beams. Liu [18] used thermal modeling to evaluate the impacts of electric heating pipe burial spacing and depth, heating power, and wind speed on the energy consumption and energy utilization of an electric heating pipe automated snow melting system. Nuijten [19] used a heated pavement snow melting model experiment to examine the melting processes of uncompressed and compressed snow, and the findings revealed that melting compacted snow takes more time and energy.

In terms of mechanical properties, Nilimaa [20] confirmed that internal heating cables may be employed in cold-weather concrete floor construction. By shortening the time it takes for concrete slabs to dehydrate in cold areas, this heating technique can strengthen the road and speed up the drying process. Nishizawa [21] examined the temperature stresses in thick concrete pavement panels by field experiments as well as 3D finite element models and provided a method to calculate the actual temperature stresses in concrete pavement in a computer field. Luccioni [22] created a thermodynamic model of concrete under high-temperature action that could mimic the residual mechanical behavior of concrete at high temperatures, including stiffness, strength loss, Poisson's ratio reduction, and inelastic behavior changes. Neuenschwander [23] validated the damage plasticity model's applicability by measuring the uniaxial characteristics of concrete under cyclic stress at high temperatures, providing fresh temperature-dependent calibration data for the damage plasticity model. Ruan [24] examined the coupling effect of high temperature and high strain rate in concrete using the finite element modeling software ABAQUS (https://www.3ds.com/products/simulia/abaqus/cae (accessed on 21 November 2023)) and a damage plastic concrete model. Chen [25] investigated the damage morphology of plain concrete under high-temperature action, and the results revealed considerable variation in the damage morphology of concrete at ambient temperature. Gawin [26] proposed an intrinsic model to study concrete deformation under transitory temperature and pressure conditions, which incorporated both thermochemical and mechanical damage. Ripani [27] established a thermodynamically consistent gradient poroplastic model for high-temperature concrete and demonstrated its prediction power for various stress routes and thermal circumstances. Sharifi [28] used Paris' rule to quantify the cumulative fatigue fracture damage of PCM-

rich concrete slabs subjected to cyclic hot bending stresses. Nilimaa [29] evaluated the danger of thermal fractures in concrete constructions. According to the findings of this study, pre-embedding heating wires before pouring the concrete construction can minimize temperature stress during the hydration process. The research in the aforementioned publications was all conducted at high temperatures outside the concrete pavement and did not examine the mechanical characteristics of concrete pavement with integrated carbon fiber heating wires.

Therefore, there is a lack of studies on the mechanical behavior of electrically heated pavement materials. This study aimed to investigate the temperature and thermal stress distributions inside concrete pavement with embedded carbon fiber heating wires through model tests and numerical simulation. The accuracy of the numerical model is verified by comparison to model test results. The analysis reveals the maximum tensile and compressive stresses generated during the heating process and their distribution characteristics. Moreover, the relationship between the temperature gradient and thermal stress is quantified. The findings can provide a reference for the design of electrically heated concrete pavement.

2. Test Introduction

2.1. Test Materials

The concrete pavement model used in this study was composed of C40 concrete. The mix proportion of the C40 concrete for the pavement was 17% cement, 27% fine aggregate, 48% coarse aggregate, 7% water, and 1% water reducer. The cement was 42.5 MPa regular silicate cement, the fine aggregate was medium sand with a fineness modulus of 3.0, the coarse aggregate was crushed stone with a grain size of 10–30 mm, and a polycarboxylate water reducer was used. After curing, the concrete model had a compressive strength (σ_c) of 46 MPa and flexural strength (σ_b) of 6 MPa. The carbon fiber heating wire used in this study was a reinforced plastic composite material.

The performance parameters of the carbon fiber heating wire are shown in Table 1.

Table 1. Performance parameters of carbon fiber heating.

Diameter	Heating Power	Resistance	Tensile Strength	Compressive Strength
8 mm	20 W/m	13 Ω/m	1.7 GPa	1.2 GPa

2.2. Test Design

In this study, the temperature and thermal strain fields generated in the concrete pavement during the heating process were investigated through a carbon fiber-heated concrete pavement model test. Model tests are commonly used to simulate actual engineering projects by embedding carbon fiber heating wires into a scaled concrete pavement model.

Figure 1 shows the dimensions of the concrete pavement model: 0.25 m in height, 0.8 m in width, and 1 m in length.

Figure 2 shows the construction process of the entire model. The heating method used in this model test was a pre-buried carbon fiber heating wire with a total length of 14 m. Concrete pavement needs to be cured after it is poured. The test model was maintained for 28 days under the environmental parameters of 10 °C ambient temperature and 60% ambient humidity. To avoid affecting the stability of the concrete pavement layer structure and achieve good snow and ice melting performance, the carbon fiber was placed at a depth of 4.2 cm in the pavement. The carbon fiber was arranged in a U-shaped circuit with a horizontal spacing of 8 cm between two neighboring carbon fibers. This configuration can reduce heat loss while increasing the heated area. The carbon fiber heating wire adopted a constant power heating method, with a constant power of 20 W/m.

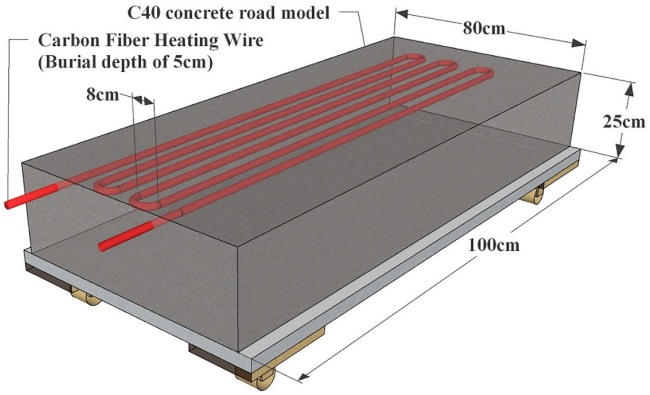

Figure 1. 3D model of carbon fiber-heated pavement.

(**a**) Tying reinforcement cages

(**b**) Laying out carbon fiber heating wire

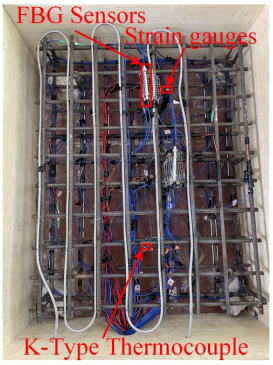

(**c**) Deploying data acquisition devices

(**d**) Pouring concrete

(**e**) Concrete complete - 28 days curing

Figure 2. Carbon fiber-heated pavement model construction process.

2.3. Test Data Acquisition

To monitor the temperature and strain distributions inside the concrete pavement during the test, four layers of data acquisition points were set up with a total of 24 temperature and strain measurement locations.

The pavement temperature was measured using K-type thermocouples. Twenty-four temperature measurement points were arranged in four layers at depths of 2 cm, 5 cm, 10 cm, and 15 cm, respectively, as shown in Figure 3. In the first layer (2 cm depth), for example, points $A_{1\text{-}1}$, $A_{1\text{-}2}$, and $A_{1\text{-}3}$ were in the vertical direction of the carbon fiber heating wire, while points $B_{1\text{-}1}$, $B_{1\text{-}2}$, and $B_{1\text{-}3}$ were in the vertical direction of the midpoint between two neighboring heating wires, as illustrated in Figure 3.The K-type thermocouple had a measurement range of −60 to 250 °C with an accuracy of 0.5 °C and a sampling interval of 30 min. The temperature data logger was manufactured by Keysight.

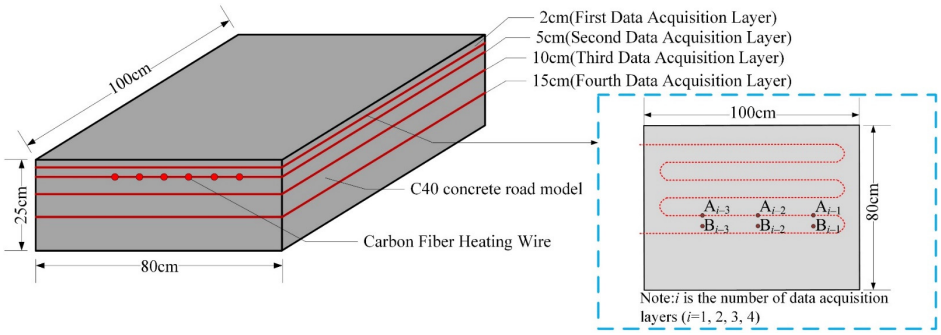

Figure 3. Distribution of data acquisition layers and data point numbers.

Similarly, 24 strain measurement points were arranged in four layers at the same depths to monitor the thermal strain evolution. In each layer, six strain gauges were installed, including three ($A_{1\text{-}1}$, $A_{1\text{-}2}$, $A_{1\text{-}3}$) in the heating wire direction and three ($B_{1\text{-}1}$, $B_{1\text{-}2}$, $B_{1\text{-}3}$) in the middle of the two wires, following the same numbering rule as the temperature points shown in Figure 3. The strain was measured using a combination of buried fiber Bragg grating (FBG) sensors (horizontal arrangement) and 120-10AA weldless steel strain gauges (vertical arrangement).

The test was carried out in a constant temperature and humidity laboratory, where the environmental parameters such as ambient temperature and wind speed could be controlled and monitored in real time.

3. Test Results and Analysis

The ambient temperature was set at −3 °C for the temperature increase test. The carbon fiber electric heating wire heated the pavement model for 6 h under these environmental conditions. The test findings were separated into temperature distribution and thermal strain distribution. To reduce test error, the temperature and strain were averaged for three A-numbered spots and three B-numbered points at the same depth. The temperature data were classified as TC_A and TC_B, while the strain data were classified as TS_A and TS_B.

3.1. Temperature Distribution of Pavement Model Test

In this section, K-type thermocouples were utilized to acquire temperature data from the pavement model during the heating process. Based on the collected data, the temperature distribution characteristics of the carbon fiber-heated pavement were analyzed.

Figure 4a,b show the warming trends in TC_A and TC_B with heating time at different depths of the pavement, respectively. The TC_A and TC_B warming trends for the same depth case can be divided into two stages: the first for the start of heating to 2 h and the second for heating 2 h to 6 h. The temperature rose faster in the first stage, then progressively slowed down in the second. Taking the 5 cm depth pavement as an example, the first-stage TC_A temperature rose from −3 °C to 5 °C with a heating rate of 4 °C/h, and the TC_B temperature rose from −3 °C to 4 °C with a heating rate of 4.75 °C/h; the second-stage TC_A temperature rose from 5 °C to 10 °C with a heating rate of 1.25 °C/h, and the TC_B temperature rose from 4 °C to 8 °C with a heating rate of 1 °C/h. The temperature of the first-stage TC_A rose from −3 °C to 5 °C at a pace of 4 °C/h, whereas the temperature of the second-stage TC_B climbed from −3 °C to 4 °C at a rate of 4.75 °C/h. According to Fourier's law, the greater the temperature difference, the greater the heat flow density and thus the faster the heating rate, whereas in the second stage, as the temperature difference between the carbon fiber heating wire and the road surface decreased, the heat flow density and thus the heating rate decreased.

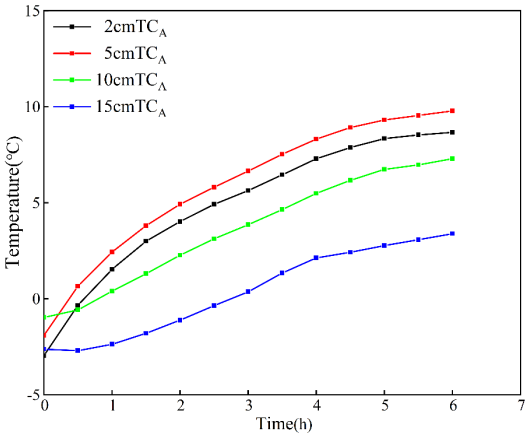

(**a**) Trend in TC$_A$ with time at different depths

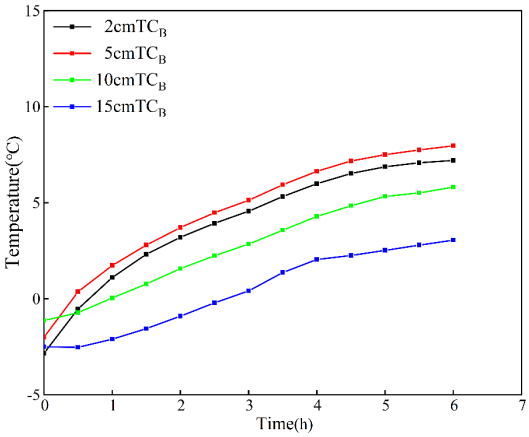

(**b**) Trend in TC$_B$ with time at different depths

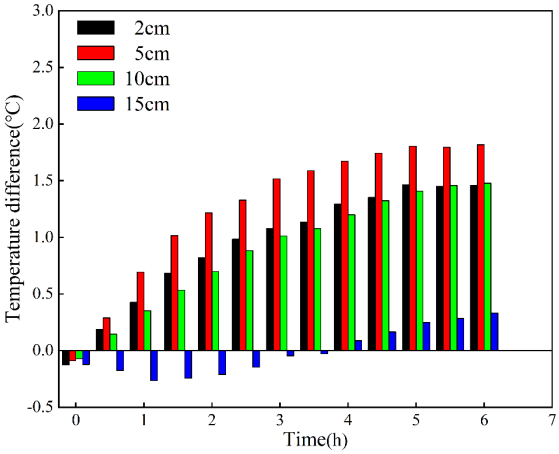

(**c**) Trend in temperature difference with time in the horizontal direction of the road surface

Figure 4. The temperature distribution properties of carbon fiber—heated pavement at various depths.

Figure 4c shows the horizontal temperature uniformity at various pavement depths, particularly the temperature difference in the horizontal direction between TC$_A$ and TC$_B$. For instance, the maximum temperature difference was 2 °C between depths of 5 cm and 15 cm, while it was 0.3 °C between depths of 15 cm and 5 cm. The results indicated that the pavement temperature became more uniform with increasing depth. During heating, temperature gradients existed in both the horizontal and vertical directions of the pavement.

Figure 5a,b illustrate how the temperature gradient evolved over time in the horizontal and vertical directions, respectively. In the horizontal direction, the temperature gradient at depths of 2 cm, 5 cm, and 10 cm all demonstrated a trend of initially rapidly increasing followed by slowing down, as shown in Figure 5a. However, the temperature differential in the horizontal direction exhibited steady linear growth at a depth of 15 cm. These trends indicated that the horizontal temperature gradient increased at a slower rate with distance away from the carbon fiber heating wire. In the vertical direction, the temperature gradients of both TC$_A$ and TC$_B$ evolved similarly—growing rapidly initially and then stabilizing after 2 h of heating, as depicted in Figure 5b. The vertical temperature gradient reached its maximum value after 2 h. This showed that the vertical temperature gradient was greater closer to the carbon fiber heating wire. According to the design specifications for highway cement concrete pavement, the temperature gradient of carbon fiber-heated pavement was much greater than the value provided in the design specification.

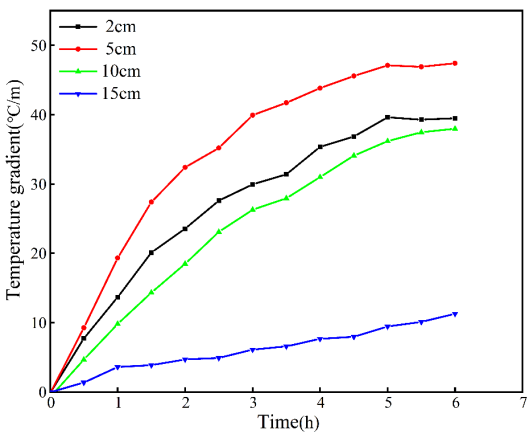

(**a**) Trend in TC$_A$ temperature gradient in horizontal direction at different depths

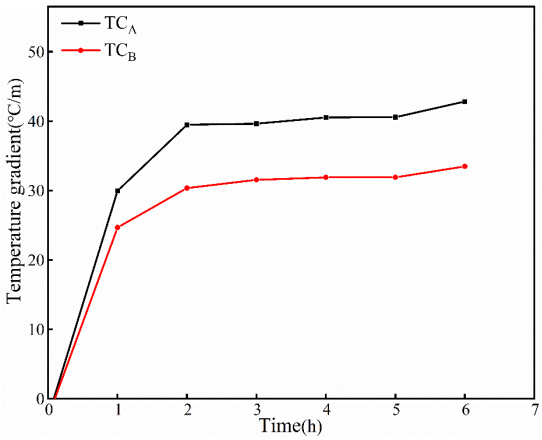

(**b**) Trends in TC$_A$ and TC$_B$ temperature gradients in depth direction

Figure 5. Trends of temperature gradients in horizontal direction and depth direction.

3.2. Thermal Strain Distribution of Pavement Model Test

In this section, Fiber Bragg Grating (FBG) sensors in combination with strain gauges were utilized to collect strain data from the pavement model during the heating process in order to analyze the thermal strain distribution in the horizontal direction. The characteristics of the thermal strain distribution in the carbon fiber-heated pavement were also investigated.

Figure 6a,b show the trends in thermal strain with heating time for TS_A and TS_B at various depths of the pavement. The thermal strain on the pavement gradually increased as the heating duration increased. The rate of growth of thermal strain decreased with increasing vertical distance from the carbon fiber heating wire. The greatest thermal strains of TS_A and TS_B, for example, were situated at a depth of 5 cm, 209 με and 192 με, respectively, and the minimum thermal strains were located at a depth of 15 cm, 86 με and 80 με, respectively. The thermal strain on the pavement near the carbon fiber heating wire is clearly of concern based on the foregoing properties.

Figure 6c shows the consistency of the pavement's thermal strain in the horizontal plane at various depths. That is, the difference in thermal strain in the horizontal direction of the pavement between TS_A and TS_B at different depths. With increasing heating time, the horizontal thermal strain difference increased, then decreased, and ultimately stabilized. The horizontal thermal strain differential increased as heating time increased, followed by a pattern of decreasing and then stabilizing. Additionally, the trend became less pronounced the further the vertical distance from the carbon fiber heating wire. For example, after 1 h of heating beneath a 5 cm deep pavement, the difference between TS_A and TS_B reached a maximum value of 80 με. With increased heating time, the difference between TS_A and TS_B gradually decreased and finally stabilized at 40 με. And the gap between TS_A and TS_B was essentially constant at around 20 με beneath 15 cm deep pavement. The above characteristics showed that as heating time and distance from the carbon fiber heating wire increased, the pavement thermal strain field became more stable.

By comparing Figures 4 and 6, it is clear that the trends in pavement temperature change and thermal strain change were essentially the same during the carbon fiber heating pavement model process. Temperature and thermal strain variations with time were more visible at a depth of 5 cm for the carbon fiber heating hot line pavement layer. As a result, the linear correlation between TV_A and TS_A was fitted and examined under 5 cm depth pavement, as shown in Figure 7. TV_A denotes the amount of TC_A change. That is, the difference in temperature between the pavement and the starting temperature at various heating periods. The fitted curve's R^2 correlation value was 0.97. The thermal strain of carbon fiber-heated pavement could be observed to be primarily driven by the difference

in pavement temperature, and the influence of the difference in pavement temperature on the thermal strain followed a linear pattern.

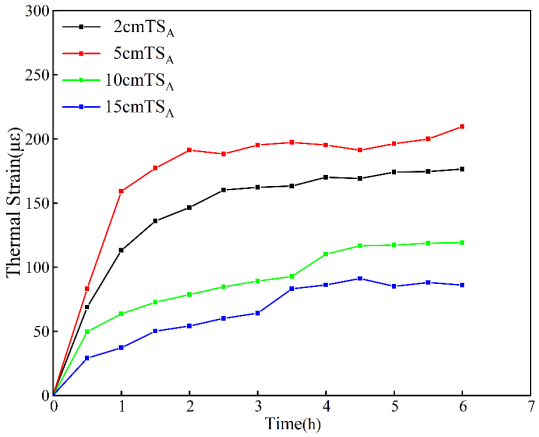

(**a**) Trend in TS$_A$ with time at different depths

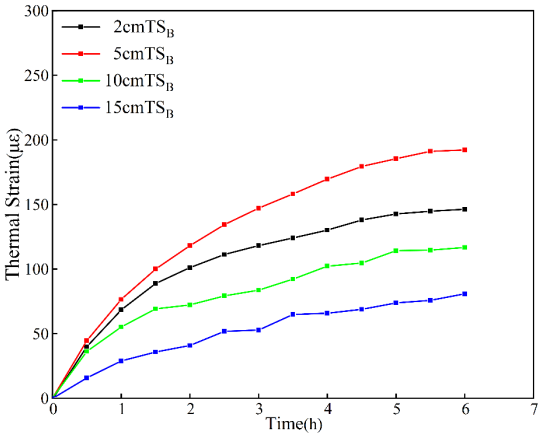

(**b**) Trend in TS$_B$ with time at different depths

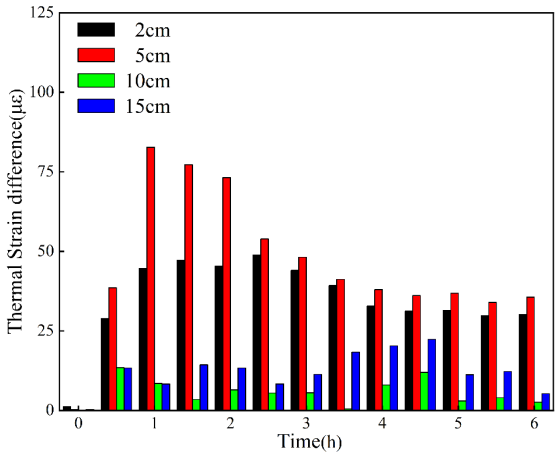

(**c**) Trend in thermal strain difference with time in the horizontal direction of the road surface

Figure 6. Heat strain distribution characteristics of carbon fiber-heated pavement at different depths.

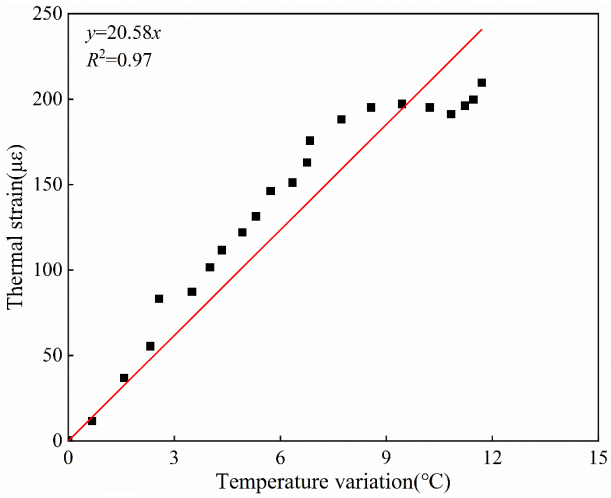

Figure 7. TV$_A$ and TS$_A$ correlation fit for 5 cm depth pavement.

4. Numerical Analysis

The numerical model analysis of the carbon fiber-heated pavement is the topic of this section. The numerical model was built using COMSOL Multiphysics 5.3 numerical simulation software to visually examine the temperature stress field of carbon fiber-heated concrete pavement, and the numerical model was verified by experimental findings.

4.1. Numerical Analysis of Governing Equations for Carbon Fiber-Heated Pavement

4.1.1. Heat Transfer Process Governing Equations

Carbon fiber heat generation is based on the principle that electrons in carbon fiber heating wires undergo energy level jumps upon activation, resulting in tiny vibrations and heat from carbon atoms. This heat is then released as far-infrared thermal radiation. Assuming a constant heating power of 20 W/m and given the speed of this operation, it is reasonable that the temperature of the carbon fiber heating filaments at different locations under the pavement remains consistent. Equation (1) was used to determine the transient heat transfer process of the carbon fiber-heated pavement. This was due to the fact that the boundary conditions change during the actual testing process, thus making the numerical model more realistic:

$$Q = \lambda \Delta T S / L \tag{1}$$

where λ is the thermal conductivity, ΔT is the temperature difference, S is the area, and L is the thickness. This equation is based on the definition in the Cartesian coordinate system that each successive point must satisfy energy conservation.

Because the surface of the model in the test is in direct contact with the air, the surface's boundary conditions must meet Equation (2):

$$Q = \varepsilon \sigma \left(T_{amb}^4 - T_2^4 \right) \tag{2}$$

where Q is the pavement model's ambient thermal radiation, ε is the surface emissivity (a fixed value of 0.93 for this research), σ is the Stefan-Boltzmann constant, T_{amb} is the ambient temperature, and T_2 is the pavement surface temperature.

Because the model's surface is in direct contact with the air during the test, there will be convective heat exchange, which must meet Equation (3).

$$q = h(T_{amb} - T_2) \tag{3}$$

where q is the heat flow density between the concrete pavement's surface and the air, and h is the convective heat transfer coefficient between the concrete pavement's surface and the air (a fixed value of 2.3 W/(m^2·K) for this study).

Because the goal of this study was to investigate heat transport within the pavement, the boundary conditions around the pavement and at the bottom were thermally insulated. Furthermore, because the model testing was conducted in a constant-temperature laboratory without the influence of sun radiation, the numerical model did not take solar radiation into account. That is, the ambient temperature was the same as the pavement's surface temperature.

4.1.2. Temperature Stress Transfer Process Governing Equations

The concrete pavement model was believed to be an elastic material in this numerical model. The thermoelasticity equations, according to elasticity mechanics, contain the equilibrium equation, geometric equation, and intrinsic equation.

Without taking into account external loads, the equilibrium equation is (4):

$$\begin{cases} \frac{\partial \sigma_x}{\partial x} + \frac{\partial \tau_{yx}}{\partial y} + \frac{\partial \tau_{zx}}{\partial z} = 0 \\ \frac{\partial \tau_{xy}}{\partial x} + \frac{\partial \sigma_y}{\partial y} + \frac{\partial \tau_{zy}}{\partial z} = 0 \\ \frac{\partial \tau_{xz}}{\partial x} + \frac{\partial \tau_{yz}}{\partial y} + \frac{\partial \sigma_z}{\partial z} = 0 \end{cases} \tag{4}$$

where σ_x is the principal stress in the x-direction (MPa), σ_y is the principal stress in the y direction (MPa), σ_z is the principal stress in the z direction (MPa), τ_{yx} is the shear stress in the yx plane (MPa), τ_{zx} is the shear stress in the zx plane (MPa), τ_{xy} is the shear stress in the xy plane (MPa), τ_{zy} is the shear stress in the zy plane (MPa), τ_{xz} is the shear stress in the xz plane (MPa), and τ_{yz} is the shear stress in the yz plane (MPa).

The geometric equation denotes the relationship between pavement strain and displacement, which may be determined using Equation (5):

$$\begin{cases} \varepsilon_x = \frac{\partial u_x}{\partial x} \\ \varepsilon_y = \frac{\partial u_y}{\partial y} \\ \varepsilon_z = \frac{\partial u_z}{\partial z} \\ \gamma_{xy} = \frac{\partial u_x}{\partial y} + \frac{\partial u_y}{\partial x} \\ \gamma_{yz} = \frac{\partial u_y}{\partial z} + \frac{\partial u_z}{\partial y} \\ \gamma_{zx} = \frac{\partial u_z}{\partial x} + \frac{\partial u_x}{\partial z} \end{cases} \tag{5}$$

where ε_x is the strain in the x direction (με), ε_y is the strain in the y direction (με), ε_z is the strain in the z direction (με), u_x is the displacement in the x direction (m), u_y is the displacement in the y direction (m), u_z is the displacement in the z direction (m), γ_{xy} is the shear strain in the xy plane, γ_{yz} is the shear strain in the yz plane, and γ_{zx} is the shear strain in the zx plane.

The current constitutive equation illustrates the relationship between pavement strain and stress, with the pavement strain containing two components generated by thermal stress and temperature change, which may be determined using Equation (6):

$$\begin{cases} \varepsilon_x = \frac{\sigma_x}{E} - \frac{\mu(\sigma_y+\sigma_z)}{E} + \alpha\Delta T \\ \varepsilon_y = \frac{\sigma_y}{E} - \frac{\mu(\sigma_z+\sigma_x)}{E} + \alpha\Delta T \\ \varepsilon_z = \frac{\sigma_z}{E} - \frac{\mu(\sigma_x+\sigma_y)}{E} + \alpha\Delta T \\ \gamma_{xy} = \frac{\tau_{xy}}{G} \\ \gamma_{yz} = \frac{\tau_{yz}}{G} \\ \gamma_{zx} = \frac{\tau_{zx}}{G} \end{cases} \tag{6}$$

where E is Young's modulus (MPa), μ is Poisson's ratio without dimension, G is the shear modulus of elasticity (MPa), α is the linear expansion coefficient (1/K), and ΔT is the temperature difference (K). The object of this study was the temperature stress inside the pavement, so the pavement was set up with fixed constraints around and at the bottom.

4.2. Numerical Modeling

4.2.1. Three-Dimensional Numerical Analysis Model

In this numerical model, 666,164 meshes were separated. Using a line heat source, the modeling of the carbon fiber heating wire was separated into 129,441 meshes.

As illustrated in Figure 8, this model used a triangular mesh element to refine the numerical model of the pavement near the carbon fiber heating wire. The overall numerical model's calculation duration and time interval were 6 h and 0.5 h, respectively. There is an ordinary mechanical adhesion connection between the carbon fiber heat wire and the interior of the concrete pavement, and this adhesion relationship achieves stability after completion of maintenance; thus, the impact on the test results was essentially minimal. As a result, this adhesion connection could be omitted in the numerical test.

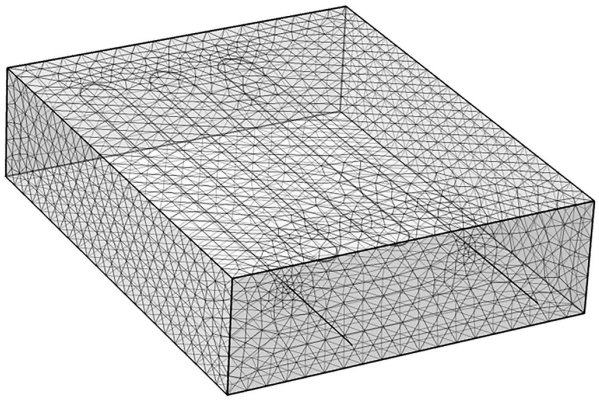

Figure 8. Schematic diagram of numerical model meshing.

4.2.2. Material Parameters Setting

For this numerical study, the ambient parameters were set to −3 °C, which was consistent with the model test. To bring the numerical analysis results closer to the model test results, the numerical model's material parameters were kept consistent with the model test material parameters.

Table 2 displays the exact specifications of the concrete pavement and carbon fiber heating wire.

Table 2. Material parameters of concrete pavement and carbon fiber heating wire.

Index	Unit	Concrete Pavement	Carbon Fiber Heating Wire
Young's modulus (E)	MPa	3.25×10^4	1.2×10^6
Poisson's ratio (μ)	–	0.2	0.2
Density (ρ)	kg/m^3	2440	1800
Thermal conductivity (λ)	W/(m·°C)	2.2	0.09
Heat capacity (c)	J/(kg·°C)	1100	900
Coefficient of linear expansion (α)	1/°C	10^{-6}	3.5×10^{-5}
Compressive strength (σ_c)	MPa	45	1.2×10^3
Tensile strength (σ_b)	MPa	5.0	1.7×10^3

4.3. Numerical Analysis Verification

This section validates the numerical model's accuracy by comparing the experimental and simulated data.

Figure 9a compares the TC_A temperature distribution in the numerical analysis results to the TC_A temperature distribution in the model test results, and Figure 9b compares the TS_A thermal strain distribution in the numerical analysis results to the TS_A thermal strain distribution in the model test results. Combined with a method of verifying the accuracy of the numerical model given in the literature [30], Table 3 shows the root mean square error (RMSE) analysis of the numerical analysis results of the temperature and strain of the pavement at different depths after 6 h of heating compared with the experimental results. The maximum root mean square errors of the pavement temperature and thermal strain were 0.7 °C and 23.82 με, respectively, which were within the error range.

The accuracy of the numerical analysis model was confirmed by the findings of this error analysis. Instrumental measurement error in the model test, as well as heat loss after energizing the carbon fiber heating wire, can create modest differences between the simulation and test findings.

Table 3. Root mean square error analysis of experimental results and simulation results.

Depth (cm)	RMSE	
	Temperature (°C)	Thermal Strain (με)
2	0.53	23.82
5	0.70	22.64
10	0.29	20.74
15	0.47	2.99

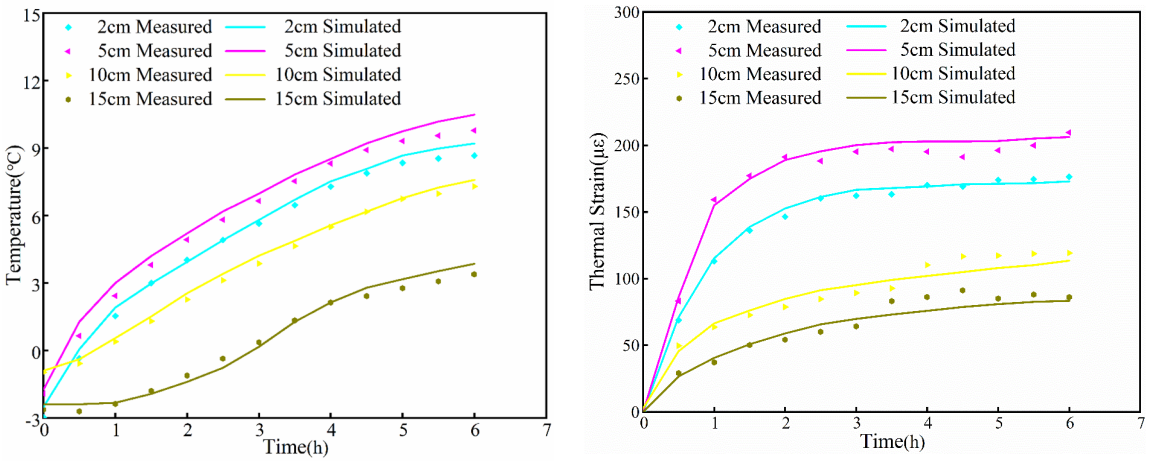

(**a**) Temperature comparison (**b**) Strain comparison

Figure 9. Comparison of test results and simulation results of TC_A and TS_A at different depths.

4.4. Distribution of Temperature Stress Field in Carbon Fiber-Heated Pavement

Since the temperature mainly varied along the depth direction in the process of heating pavement with carbon fiber, the component of the principal stress along the depth direction (later referred to as the temperature stress) was chosen for the temperature stress studied in this paper to assess the safety of the heating process. Based on the above numerical model, this section investigates the temperature stress field distribution of concrete pavement heated by carbon fiber heating wire.

Figure 10 depicts a cloud image of the temperature stress field fluctuation for various heating periods. The compressive stress was greater than the tensile stress. The stresses were mostly dispersed at the carbon fiber hairline at 0 h of heating, and the tensile and compressive stresses were quite minor. The maximum tensile and compressive stresses were 0.01 MPa and 0.06 MPa, respectively. Temperature stress was essentially non-existent in other areas of the pavement. The tensile and compressive stresses exhibited a tendency of initially rising and then stabilizing with an increase in heating time. The compressive tension around the carbon fiber heating wire steadily rose and expanded in all directions after 2 h of heating. The compressive tension decreased with increasing distance from the carbon fiber hairline and eventually turned into tensile stress. The aforementioned characteristics demonstrated that while the road surface closest to the carbon fiber hot line warmed up first, the road surface farther away did not warm up as quickly. This created a temperature gradient that caused the concrete road surface to heat unevenly, subjecting the concrete road surface's thermal expansion to the limitations of the surrounding concrete road surface. The result was compressive stresses on the road surface closest to the carbon fiber hot line and tensile stresses in the area between the two carbon fibers. Compressive stress, which was mostly spread close to the carbon fiber hairline, was the pavement's highest stress.

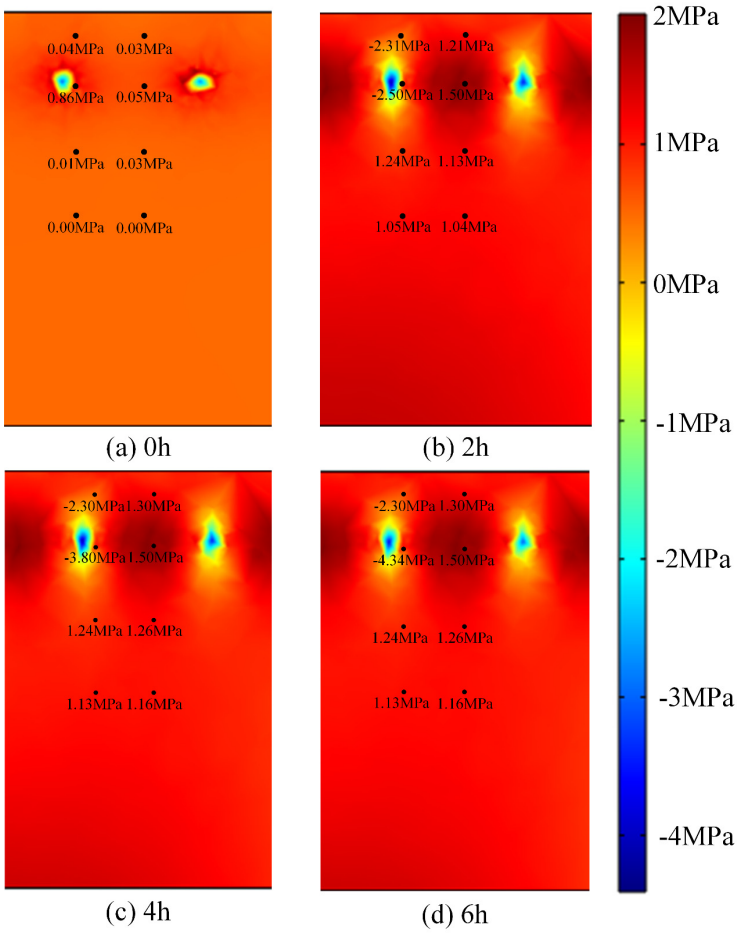

Figure 10. The numerical model of carbon fiber−heated pavement's temperature stress field distribution at different times.

Figure 11 depicts the temperature stress trend over time in the presence of carbon fiber heating wires at various depths. The carbon fiber heating wires were buried in the concrete pavement at a depth of 5 cm. The thermal stress of the pavement at various depths increased and then smoothed out over time. The pavement, for example, was subjected to compressive stress at a depth of 5 cm, and temperature stress was greatest at this level. The compressive stress increased quickly from 0 MPa to 4 MPa with a rate of 4 MPa/h during heating from 0 h to 1 h. After 1 h of heating, the compressive stress was stabilized at 4 MPa when the heating duration was increased. According to the warming trend, 6 h of heating time did not stabilize the temperature of the pavement model, and the temperature continued to rise, although at a slower pace, so the compressive stress remained stable at around 4 MPa. The maximum tensile stress of 1 MPa and maximum pressure of 4 MPa were both less than the design value of compressive strength of C40 concrete pavement in the concrete pavement design specification, indicating that the concrete pavement was safe in the carbon fiber heating process.

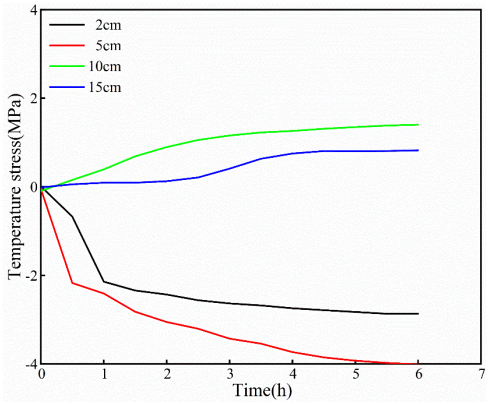

Figure 11. Trend of temperature stress of A−numbered pavement at different depths.

4.5. Analysis of Temperature Gradients and Temperature Stresses in Carbon Fiber-Heated Pavement

The link between the temperature gradient in the depth direction (hereinafter referred to as the temperature gradient) and the temperature stress is the topic of this section.

The temperature gradient and temperature stress patterns were extremely similar, as seen in Figure 12.

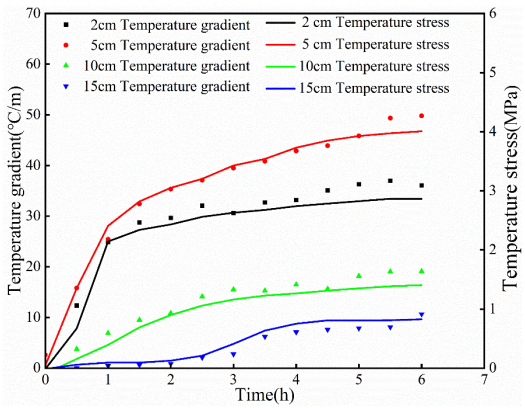

Figure 12. Temperature gradient versus temperature stress with time.

To further examine the relationship between the temperature gradient and temperature stress, the correlation between the two was fitted, as shown in Figure 13. The fitted linear interpolation yielded an excellent correlation coefficient (R^2) of 0.995. This confirmed that the temperature gradient in the carbon fiber-heated pavement was the predominant cause of temperature stress. Moreover, the temperature gradient exhibited a linear relationship with thermal stress. Taking the horizontal direction as an example, the linear correlation between temperature gradient and thermal stress at the same depth is expressed in Equation (7):

$$\sigma_T = 2.523E\alpha\Delta S\Delta T \tag{7}$$

where σ_T is the temperature stress (MPa), ΔT is the temperature gradient (°C/m), E is the Young's modulus (MPa), α is the linear expansion coefficient (1/°C), and ΔS is the distance between data points numbered A and numbered B in the same horizontal direction (fixed at 4 cm). The concrete pavement was assumed to be isotropic in this model, and the temperature stress equation was calculated using the Westcard–Bradbury method in conjunction with the above Equation (7) to obtain the temperature gradient and temperature stress relationship equation for carbon fiber-heated concrete pavement at various depths, as shown in Equation (8).

$$\sigma_T = \frac{E\alpha(|h_0 - h|)\Delta T}{2} \times 5.046 \tag{8}$$

where h_0 is the carbon fiber burial depth (m), h is the pavement depth (m), and 5.046 is the temperature stress factor.

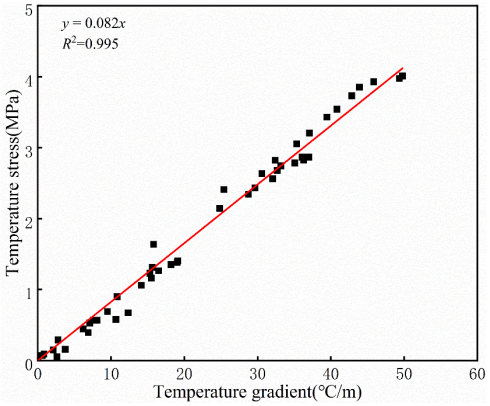

Figure 13. Pavement temperature gradient and temperature stress fitting.

The temperature stresses at different depths of pavement can be estimated using the above equation during carbon fiber heating of concrete pavement. This simplified mathematical approach can be used as a reference for real-world tasks.

5. Conclusions

The article uses numerical and modeling studies to evaluate the temperature stresses (in the depth direction) caused by heating pavement with carbon fiber. The following are the primary conclusions:

1. The trends in the thermal strain field and temperature field from the model tests are typically similar, and the fitted correlation between the two implies that temperature changes cause thermal strains to occur.
2. The temperature gradient of carbon fiber-heated pavement is significantly greater than the value stated in the concrete pavement design standard. The horizontal temperature gradient is greater than the vertical temperature gradient. This demonstrates the importance of studying the temperature stress of carbon fiber-heated pavement.
3. The temperature stresses within carbon fiber-heated pavement were investigated along the depth direction in the numerical model testing. Root mean square error (RMSE) analysis of the model test results and numerical test results proved the accuracy of the numerical model of carbon fiber-heated pavement.
4. It was shown that the temperature gradient causes the temperature stress by fitting the relationship between the temperature gradient and temperature stress for pavement at various depths. Furthermore, to offer recommendations for real-world engineering applications, a linear equation for the temperature gradient and temperature stress in the depth direction is offered.

The study's findings may be utilized to guide and optimize the structural design and construction of carbon fiber-heated concrete pavement, as well as to review the safety performance and structural integrity of this pavement.

Author Contributions: Conceptualization, N.Z., Z.C. and H.X.; methodology, Z.C.; software, N.Z.; validation, N.Z., Z.C. and H.X.; formal analysis, N.Z.; investigation, Z.C.; resources, H.X.; data curation, N.Z.; writing—original draft preparation, N.Z.; writing—review and editing, Z.C. and L.Z.; visualization, N.Z.; supervision, Z.C., H.X. and L.Z.; project administration, Z.C., H.X., L.Z. and Q.M.; funding acquisition, Z.C., H.X., L.Z. and Q.M. All authors have read and agreed to the published version of the manuscript.

Funding: This work was supported by the Key Research and Development Program of Hubei Province (No. 2021BGD015) and the Technology Innovation Project of Hubei Province (No. 2023BEB010).

Institutional Review Board Statement: Not applicable.

Informed Consent Statement: Not applicable.

Data Availability Statement: The data presented in this study are available upon request from the corresponding author. The data are not publicly available due to copyright issues with co-developers.

Conflicts of Interest: The authors declare that the research was conducted in the absence of any commercial or financial relationships that could be construed as potential conflicts of interest.

References

1. Arvidsson; Anna, K. The Winter Model—A new way to calculate socio-economic costs depending on winter maintenance strategy. *Cold Reg. Sci. Technol.* **2017**, *136*, 30–36. [CrossRef]
2. Gutchess, K.; Jin, L.; Lautz, L.; Shaw, S.B.; Zhou, X.; Lu, Z. Chloride sources in urban and rural headwater catchments, central New York. *Sci. Total Environ.* **2016**, *565*, 462–472. [CrossRef] [PubMed]
3. Balbay, A.; Esen, M. Experimental investigation of using ground source heat pump system for snow melting on pavements and bridge decks. *Sci. Res. Essays* **2010**, *5*, 3955–3966.
4. Yu, X.; Hurley, M.T.; Li, T.; Lei, G.; Pedarla, A.; Puppala, A.J. Experimental feasibility study of a new attached hydronic loop design for geothermal heating of bridge decks—ScienceDirect. *Appl. Therm. Eng.* **2019**, *164*, 114507. [CrossRef]
5. Kim, H.S.; Ban, H.; Park, W.J. Deicing Concrete Pavements and Roads with Carbon Nanotubes (CNTs) as Heating Elements. *Materials* **2020**, *13*, 2504. [CrossRef]
6. Lai, J.X.; Liu, C.; Gong, C.B. Research Situation and Prospect for Highway Snowmelt Deicing Technology with Electric Heat Tracing. *Appl. Mech. Mater.* **2011**, *71–78*, 1865–1869. [CrossRef]
7. Wang, K.; Nelsen, D.E.; Nixon, W.A. Damaging effects of deicing chemicals on concrete materials. *Cement Concrete Comp.* **2006**, *28*, 173–188. [CrossRef]
8. Thunqvist, E.L. Regional Increase of Mean Chloride Concentration in Water Due to the Application of Deicing Salt. *Sci. Total Environ.* **2004**, *325*, 29–37. [CrossRef]
9. Buss, N.; Nelson, K.N.; Hua, J.; Relyea, R.A. Effects of different roadway deicing salts on host-parasite interactions: The importance of salt type. *Environ. Pollut.* **2020**, *266*, 115244. [CrossRef]
10. Liu, K.; Huang, S.; Xie, H.; Wang, F. Multi-objective optimization of the design and operation for snow-melting pavement with electric heating pipes. *Appl. Therm. Eng.* **2017**, *122*, 359–367. [CrossRef]
11. Vignisdóttir, H.R.; Booto, G.K.; Bohne, R.A.; Bratteb, H.; O'Born, R. A review of environmental impacts of winter road maintenance. *Cold Reg. Sci. Technol.* **2018**, *158*, 143–153. [CrossRef]
12. Zhao, H.; Wu, Z.; Wang, S.; Zheng, J.; Che, G. Concrete pavement deicing with carbon fiber heating wires. *Cold Reg. Sci. Technol.* **2011**, *65*, 413–420. [CrossRef]
13. Lai, Y.; Liu, Y.; Su, X.; Ma, D.X.; Wang, P. The influence of heat flux on melting ice on concrete pavement with carbon fibre heating wire. *IOP Conf.* **2018**, *392*, 022021. [CrossRef]
14. Lai, Y.; Liu, Y.; Ma, D. Automatically melting snow on airport cement concrete pavement with carbon fiber grille. *Cold Reg. Sci. Technol.* **2014**, *103*, 57–62. [CrossRef]
15. Liu, K.; Huang, S.; Jin, C.; Xie, H.; Wang, F. Prediction models of the thermal field on ice-snow melting pavement with electric heating pipes. *Appl. Therm. Eng.* **2017**, *120*, 269–276. [CrossRef]
16. Qin, Y.; Hiller, J.E. Modeling temperature distribution in rigid pavement slabs: Impact of air temperature. *Construct. Build. Mater.* **2011**, *25*, 3753–3761. [CrossRef]
17. Gao, W.Y.; Dai, J.G.; Teng, J.G.; Chen, G.M. Finite element modeling of reinforced concrete beams exposed to fire—ScienceDirect. *Eng. Struct.* **2013**, *52*, 488–501. [CrossRef]
18. Liu, K.; Huang, S.; Wang, F.; Xie, H.; Lu, X. Energy consumption and utilization rate analysis of automatically snow-melting system in infrastructures by thermal simulation and melting experiments—ScienceDirect. *Cold Reg. Sci. Technol.* **2017**, *138*, 73–83. [CrossRef]
19. Nuijten, A.D.W.; Hoyland, K.V. Comparison of melting processes of dry uncompressed and compressed snow on heated pavements. *Cold Reg. Sci. Technol.* **2016**, *129*, 69–76. [CrossRef]
20. Nilimaa, J.; Zhaka, V. Material and Environmental Aspects of Concrete Flooring in Cold Climate. *Construct. Mater.* **2023**, *3*, 180–201. [CrossRef]
21. Nishizawa, T.; Ozeki, T.; Katoh, K.; Matsui, K. Finite Element Model Analysis of Thermal Stresses of Thick Airport Concrete Pavement Slabs. *Transp. Res. Record J. Transp. Res. Board.* **2009**, *2095*, 3–12. [CrossRef]
22. Luccioni, B.M.; Figueroa, M.I.; Danesi, R.F. Thermo-mechanic model for concrete exposed to elevated temperatures. *Eng. Struct.* **2003**, *25*, 729–742. [CrossRef]
23. Neuenschwander, M.; Knobloch, M.; Fontana, M. Suitability of the damage-plasticity modelling concept for concrete at elevated temperatures: Experimental validation with uniaxial cyclic compression tests. *Cement Concrete Res.* **2016**, *79*, 57–75. [CrossRef]
24. Ruan, Z.; Chen, L.; Fang, Q. Numerical investigation into dynamic responses of RC columns subjected for fire and blast. *J. Loss Prevent Proc.* **2015**, *34*, 10–21. [CrossRef]

25. Chen, L.; Fang, Q.; Jiang, X.; Ruan, Z.; Hong, J. Combined effects of high temperature and high strain rate on normal weight concrete. *Int. J. Impact Eng.* **2015**, *86*, 40–56. [CrossRef]
26. Gawin, D.; Pesavento, F.; Schrefler, B.A. Modelling of deformations of high strength concrete at elevated temperatures. *Mater. Struct.* **2004**, *37*, 218–236. [CrossRef]
27. Ripani, M.; Etse, G.; Vrech, S.; Mroginski, J. Thermodynamic gradient-based poroplastic theory for concrete under high temperatures. *Int. J. Plasticity* **2014**, *61*, 157–177. [CrossRef]
28. Sharifi, N.P.; Askarinejad, S.; Mahboub, K.C. Fracture performance of a PCM-Rich concrete pavement under thermal stresses. *Int. J. Pavement Eng.* **2020**, *23*, 221–230. [CrossRef]
29. Nilimaa, J.; Hsthagen, A.; Emborg, M. Thermal Crack Risk of Concrete Structures–Evaluation of Theoretical Models for Tunnels and Bridges. *Nordic Concrete Res.* **2017**, *56*, 55–69.
30. Nowoświat, A.; Olechowska, M. Experimental Validation of the Model of Reverberation Time Prediction in a Room. *Buildings* **2022**, *12*, 347. [CrossRef]